Aug. 2007 version, accepted for publication to JAMC

A Midlatitude Precipitating Cloud Database Validated with Satellite Observations

JEAN-PIERRE CHABOUREAU,[*] NATHALIE SÖHNE,[*] JEAN-PIERRE PINTY,[*]
INGO MEIROLD-MAUTNER,[+] ERIC DEFER,[+] CATHERINE PRIGENT,[+]
JUAN R. PARDO,[#] MARIO MECH,[@] AND SUSANNE CREWELL[@]

[*]*Laboratoire d'Aérologie, Université Paul Sabatier and CNRS, Toulouse, France*
[+]*LERMA, Observatoire de Paris, Paris, France*
[#]*Instituto de Estructura de la Materia, CSIC, Madrid, Spain*
[@]*Institute for Geophysics and Meteorology at the University of Cologne, Germany*

ABSTRACT

The simulations of five midlatitude precipitating events by the non-hydrostatic mesoscale model Meso-NH are analyzed. These cases cover contrasted precipitation situations from 30 to 60° N, which are typical of midlatitudes. They include a frontal case with light precipitation over the Rhine area (10 February 2000), a long lasting precipitation event at Hoek van Holland (19 September 2001), a moderate rain case over the Elbe (12 August 2002), an intense rain case over Algiers (10 November 2001), and the 'millennium storm' in England (30 October 2000). The physically consistent hydrometeor and thermodynamic outputs are used to generate a database for cloud and precipitation retrievals. The hydrometeor vertical profiles generated vary mostly with the 0° C isotherm, located between 1 and 3 km height depending on the case. The characteristics of this midlatitude database are complementary to the GPROF database, which mostly concentrates on tropical situations.

The realism of the simulations is evaluated against satellite observations by comparing synthetic brightness temperatures (BTs) with Advanced Microwave Sounding Unit (AMSU), Special Sensor Microwave Imager (SSM/I), and METEOSAT observations. The good reproduction of the BT distributions by the model is exploited by calculating categorical scores for verification purposes. The comparison with three-hourly METEOSAT observations demonstrates the ability of the model to forecast the time evolution of the cloud cover, the latter being better predicted for the stratiform cases than for others. The comparison with AMSU-B measurements shows the skill of the model to predict rainfall at correct location.

1. Introduction

Research efforts are continuing in the aim of improving the modeling of cloud and precipitation processes, for both climate monitoring and weather forecasting. As for many geophysical variables, observation of cloud and precipitation is possible at global scale by remote sensing from space only. In particular, retrieving rain rates is a motivation of passive microwave measurements from satellites in low earth orbit like the Special Sensor Microwave Imager (SSM/I) operational series and the Tropical Rainfall Measuring Mission (TRMM). Future programs are envisioned to observe global precipitation more frequently and more accurately by using a constellation of passive microwave radiometers as in Global Precipitation Measurement (GPM) or by developing systems observing in the submillimeter spectral range from geostationary platforms.

Microwave measurements do not directly sense surface rain rates but are often sensitive to the full atmospheric column, including the various cloud layers. Precipitating cloud databases have been built to investigate the relationship between space-borne measurements and rainfall (e.g., Bauer 2001; Kummerow et al. 2001; Panegrossi et al. 1998). These precipitating cloud databases are composed of thousands of physically consistent hydrometeor and thermodynamic profiles obtained from cloud-resolving model simulations. Brightness temperatures (BTs) are computed from these simulated cloud profiles, using a radiative transfer

Corresponding author address:
Dr. Jean-Pierre Chaboureau, Laboratoire d'Aérologie, Observatoire Midi-Pyrénées, 14 av. Belin, F-31400 Toulouse, France.
E-mail: jean-pierre.chaboureau@aero.obs-mip.fr

model (RTM). The relationships between the atmospheric variables in the model and the simulated BTs are then used to develop inversion procedures to retrieve cloud and precipitation fields from a set of satellite observations. An advantage of these mesoscale databases is that they provide profiles with a more detailed description of the microphysics than the low-resolution Numerical Weather Prediction (NWP) can give, and associated with realistic synthetic BTs obtained from state-of-the art RTMs.

The existing databases mainly sample tropical situations under convective conditions. For example, the GPROF (Goddard PROFiling) database was built to retrieve rain from both SSM/I and TRMM observations. As noted by Kummerow et al. (2001), all the model simulations in the GPROF database (its first version) are tropical in nature and, in most of them, stratiform rain events are represented in close proximity to convection. As a consequence, such databases cannot be directly used to develop algorithms for rainfall estimates outside the tropics. (Note however that the latest version of the GPROF database contains also two midlatitude simulations (Olson et al. 2006).) This motivated us to perform realistic simulations for a variety of extratropical environments. Furthermore, surface rain retrieval methods are very sensitive to the database from which the inversion algorithm is generated. For example, Medaglia et al. (2005) investigate this issue for two models having different bulk microphysical schemes showing significant differences in the retrieved rain rates. This underlines the need to evaluate the simulated database, in particular with the existing satellite observations.

In this study, we propose a database of midlatitude profiles obtained from situations over Europe and the Mediterranean Sea simulated by the non-hydrostatic mesoscale model Meso-NH (Lafore et al. 1998). This database can be used for many purposes: to test the ability of the Meso-NH model coupled with radiative transfer codes to simulate realistic BTs (Meirold-Mautner et al. 2007), to quantify the skill of the model to forecast midlatitude rain events (this study), to retrieve hydrometeor contents from existing satellite observations, and to investigate the capabilities of future sensors in the submillimeter range (Defer et al. 2007; Mech et al. 2007).

Five typical midlatitude cases have been identified. They cover large domains in the latitudes 30-60° N providing a large number of heterogeneous profiles with various microphysical compositions. The cases correspond to real meteorological conditions, allowing an evaluation of the quality of the simulated hydrometeor fields by comparison with coincident satellite observations. This is the model-to-satellite approach (Morcrette 1991) in which the satellite BTs are directly compared to the BTs computed from the predicted model fields. Using this method, the meteorological model coupled with the radiative transfer code can be evaluated before developing any rainfall retrieval from the simulated database. Previous studies have assessed the Meso-NH model cloud scheme in terms of cloud cover and hydrometeor contents by comparison with METEOSAT (Chaboureau et al. 2000, 2002; Meirold-Mautner et al. 2007), GOES (Chaboureau and Bechtold 2005), TRMM Microwave Imager (TMI) (Wiedner et al. 2004), SSM/I and Advanced Microwave Sounding Unit (AMSU) (Meirold-Mautner et al. 2007) observations. The model-to-satellite approach associated with the BT difference technique applied to METEOSAT Second Generation observations can also verify specific forecasts such as cirrus cover (Chaboureau and Pinty 2006), dust occurrence (Chaboureau et al. 2007b), and convective overshoots (Chaboureau et al. 2007a). Here, the evaluation is performed by comparison with observations from the METEOSAT Visible and InfraRed Imager (MVIRI), the SSM/I hosted by the Defense Meteorological Satellite Program's satellites, and the AMSU on board National Oceanic and Atmospheric Administration (NOAA) satellites. The channels most sensitive to cloud and precipitation fields, 11 μm in the infrared and 37, 85, 89, and 150 GHz in the microwave region, were selected.

The model was initialized with standard analyses on a 40-km grid mesh. Two-way interactive grid nesting was used for downscaling from the synoptic scale to the convective scale to be resolved. Typical tropical precipitating cases require a kilometer mesh to represent the convective updrafts and the associated microphysical fields explicitly. In contrast, midlatitude rain events are often more stratiform and their vertical circulation can be easily captured on a mesh with a 10-km or more grid spacing (but embedded convection in frontal rainbands needs a finer mesh to be represented realistically). Here, the setup of the simulations depended on the meteorological case. However all the model outputs were analyzed on the 10-km grid mesh, which was comparable with the spatial resolution of the satellite microwave observations used in this study. This set-up allows us to present an original application of the model-to-satellite approach by calculating categorical scores from observed and simulated BTs.

The paper is organized as follows. Section 2 presents the Meso-NH model and its mixed-phase microphysical scheme, together with the radiative codes used to calculate the BTs. Section 3 contains an overview of the cases that compose the database. Section 4 describes the variability of the database in terms of cloud and precipitation fields. The database is also contrasted with the GPROF tropical database. Section 5 evaluates the simulations by comparing the simulated BTs from Meso-NH outputs with the observed BTs from METEOSAT, SSM/I, and AMSU-B. Section 6 concludes the paper.

2. Meteorological and radiative transfer models

a. Meso-NH model and set-up

Meso-NH is a non-hydrostatic mesoscale model, jointly developed by Météo-France and the Centre National de la Recherche Scientifique (CNRS). Its general characteristics and the specific parameters for this study are summarized in Table 1. A detailed description of Meso-NH is given in Lafore et al. (1998) and the mixed-phase microphysical scheme developed by Pinty and Jabouille (1998) is described in detail in the next subsection.

Five numerical experiments are discussed in this study (Table 2). For all of them, temperature, winds, surface pressure, water vapor, and sea surface temperature taken from the European Center for Medium range Weather Forecasts (ECMWF) analysis at synoptic times (00, 06, 12, and 18 UTC) are used as initial and boundary conditions. All the simulations start at 00 UTC and use the two-way grid-nesting technique (Stein et al. 2000). The same parameterized physics are used for all the nested grids, except for convection parameterization which is not activated in the innermost grid (explicit cloud only). Results presented here are from the second grid only at 10-km resolution. The second grid covers 1600 km $\times$ 1600 km for the RHINE, HOEK, and ELBE cases, 2000 km $\times$ 1500 km for the ALGER case, and 2340 km $\times$ 2106 km for the UKMIL case. Two output times are selected for each case, corresponding to the AMSU and SSM/I pass times (Table 2).

TABLE 1. General characteristics for the simulations.

Nesting geometry	3 models *
Nested grid spacing	40, 10, 2.5 km +
Vertical grid	50 strechted levels with Δz from 60 m to 600 m
Model Top	20 km
Physical parameterizations #	
Microphysics	Bulk scheme, 5 hydrometeor species: cloud water, rain water, pristine ice, snow, graupel (Pinty and Jabouille 1998)
Radiation	ECMWF package (Gregory et al. 2000)
Turbulence	1.5-order scheme (Cuxart et al. 2000)
Surface	ISBA scheme (Noilhan and Planton 1989)

* 2 models only for the UKMIL case
+ 40 and 13 km for the UKMIL case
# These physical parameterizations correspond to the # high-resolution model. Physical parameterizations for the coarse resolution models are the same, but with the addition of a convective scheme (Bechtold et al. 2001)

b. Summary of the mixed-phase microphysical scheme

The calculations essentially follow the approach of Lin et al. (1983): a three-class ice parameterization is used with a Kessler's scheme for the warm processes. As illustrated in Fig. 1, the scheme predicts the evolution of the mixing ratios of six water species: r_v (vapor), r_c, and r_r (cloud droplets and rain drops) and r_i, r_s, and r_g (pristine ice, snow/aggregates, and frozen drops/graupel defined by an increasing degree of riming). The concentration of the pristine ice crystals, here assumed to be plates, is diagnosed. The concentration of the precipitating water drops and ice crystals (snow and graupel) is parameterized according to Caniaux et al. (1994), with the total number concentration N given by:

$$N = C\lambda^x, \tag{1}$$

where λ is the slope parameter of the size distribution, and C and x are empirical constants derived from radar observations. The size distribution of the hydrometeors is assumed to follow a generalized γ-law:

$$\begin{aligned} n(D)dD &= Ng(D)dD \\ &= N\frac{\alpha}{\Gamma(\nu)}\lambda^{\alpha\nu}D^{\alpha\nu-1}exp\big(-(\lambda D)^{\alpha}\big)dD \end{aligned} \tag{2}$$

where $g(D)$ is the normalized form which reduces to the Marshall-Palmer law when $\alpha = \nu = 1$ (D is the diameter of the drops or the maximal dimension of the particles). Finally, simple power laws are taken for the mass-size ($m = aD^b$) and for the velocity-size ($v = cD^d$) relationships to perform useful analytical integrations using the moment formula:

$$M(p) = \int_0^\infty D^p g(D)dD = \frac{\Gamma(\nu + p/\alpha)}{\Gamma(\nu)}\frac{1}{\lambda^p}, \tag{3}$$

where $M(p)$ is the p^{th} moment of $g(D)$. A first application of (3) is to compute the mixing ratio r_x as:

$$\rho r_x = aNM_x(b) \tag{4}$$

Table 3 provides the complete characterization of each ice category and cloud droplets/raindrops.

Hydrometeors are formed and destroyed according to the processes depicted in Fig. 1. The warm part of the scheme (Kessler scheme) includes the growth of cloud droplets by condensation (CND) and the formation of rain by autoconversion (AUT). Raindrops grow by accretion (ACC) or evaporate in subsaturated areas (EVA).

In the cold part of the scheme, the pristine ice category is initiated by homogeneous nucleation (HON) when

TABLE 2. Overview of the simulation cases.

Name	Event	Date	AMSU id (Time)	SSM/I id (Time)
RHINE	Light precipitation over Rhine	10 Feb. 2000	N15 (18 UTC)	F14 (09 UTC)
HOEK	Light rain at Hoek van Holland	19 Sept. 2001	N15 (18 UTC)	F14 (09 UTC)
ELBE	Elbe flood	12 Aug. 2002	N15 (06 UTC)	F14 (18 UTC)
ALGER	Algiers flood	10 Nov. 2001	N15 (02 UTC)	F14 (07 UTC)
UKMIL	'Millennium storm'	30 Oct. 2000	N15 (09 UTC)	F13 (06 UTC)

TABLE 3. Characteristics of each hydrometeor category.*

Parameters	r_i	r_s	r_g	r_c	r_r
α	3	1	1	3	1
ν	3	1	1	3	1
a	0.82	0.02	19.6	524	524
b	2.5	1.9	2.8	3	3
c	800	5.1	124	$3.2\ 10^7$	842
d	1.00	0.27	0.66	2	0.8
C		5	$5\ 10^5$		10^7
x		1	-0.5		-1

* Coefficients α and ν are used in Eq. (2). The other coefficients are related to power law relationships for the mass ($m = aD^b$), and the fall speed ($v = cD^d$), where D is the particle size, and for the concentration in Eq. (1). All variables are in MKS units.

T$\leq -35^\circ$ C, or more frequently by heterogeneous nucleation (HEN), so the small ice crystal concentration is a simple function of the local supersaturation over ice. These crystals grow by water vapor deposition (DEP) and by the Bergeron-Findeisen effect (BER). The snow phase is formed by autoconversion (AUT) of the primary ice crystals; it grows by deposition (DEP) of water vapor, by aggregation (AGG) through small crystal collection, and by the light riming produced by impaction of cloud droplets (RIM) and raindrops (ACC). Graupel are formed as a consequence of the heavy riming of snow (RIM and ACC) or by rain freezing (CFR) when supercooled raindrops come into contact with pristine ice crystals. The distinction between light and heavy riming is made on the basis of a critical size of the snowflakes (droplets) or by estimation of the mean density of the resulting particles (raindrops). According to the heat balance equation, graupel can grow more efficiently in the WET mode than in the DRY mode when riming is very intense (as for hailstone embryos). In the latter case, the excess of non-freezable liquid water at the surface of the graupel is shed (SHD) to form raindrops. When T$\geq 0^\circ$ C, pristine crystals immediately melt into cloud droplets (MLT) while snowflakes are progressively converted (CVM) into graupel that melt (MLT) as they fall. Each condensed water species has a non-zero fall speed except for cloud droplets.

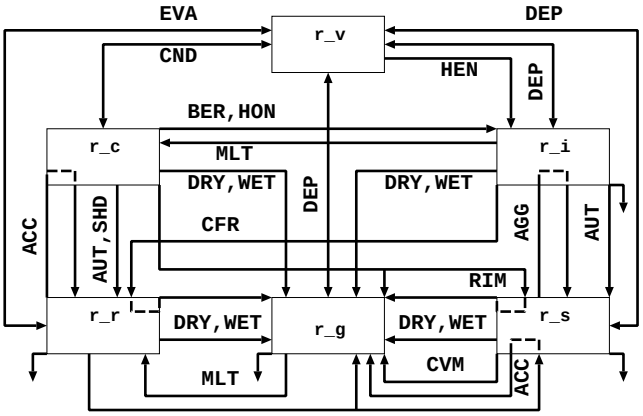

FIG. 1. Microphysical processes included in the mixed-phase scheme (see text for the acronyms and explanations).

c. Radiative transfer models

Synthetic BT corresponding to the METEOSAT-7 infrared channel in the thermal infrared window (10.5-12.5 μm, hereafter referred to as 11 μm) were computed using the Radiative Transfer for the Tiros Operational Vertical Sounder (RTTOV) code version 8.7 (Saunders et al. 2005). In the infrared, the RTTOV code takes clouds into account as grey bodies (Chevallier et al. 2001). Hexagonal columns are assumed with radiative properties taken from Baran and Francis (2004) and with an effective dimension diagnosed from the ice water content (McFarquhar et al. 2003). The surface emissivity over land is given by the Ecoclimap database (Masson et al. 2003).

In the microwave region, BT were simulated using the Atmospheric Transmission at Microwaves (ATM) model (Pardo et al. 2001; Prigent et al. 2001). Absorption by atmospheric gases was introduced according to Pardo et al. (2001) while scattering by hydrometeors was computed following the T-matrix approach of Mishchenko (1991). The sensitivity of the radiative transfer model to the characteristics of the frozen particles (size, density, dielectric properties) for the microphysics dataase presented here has been carefully analyzed in Meirold-Mautner et al. (2007). Spherical shapes are assumed for all the particles as the BT sen-

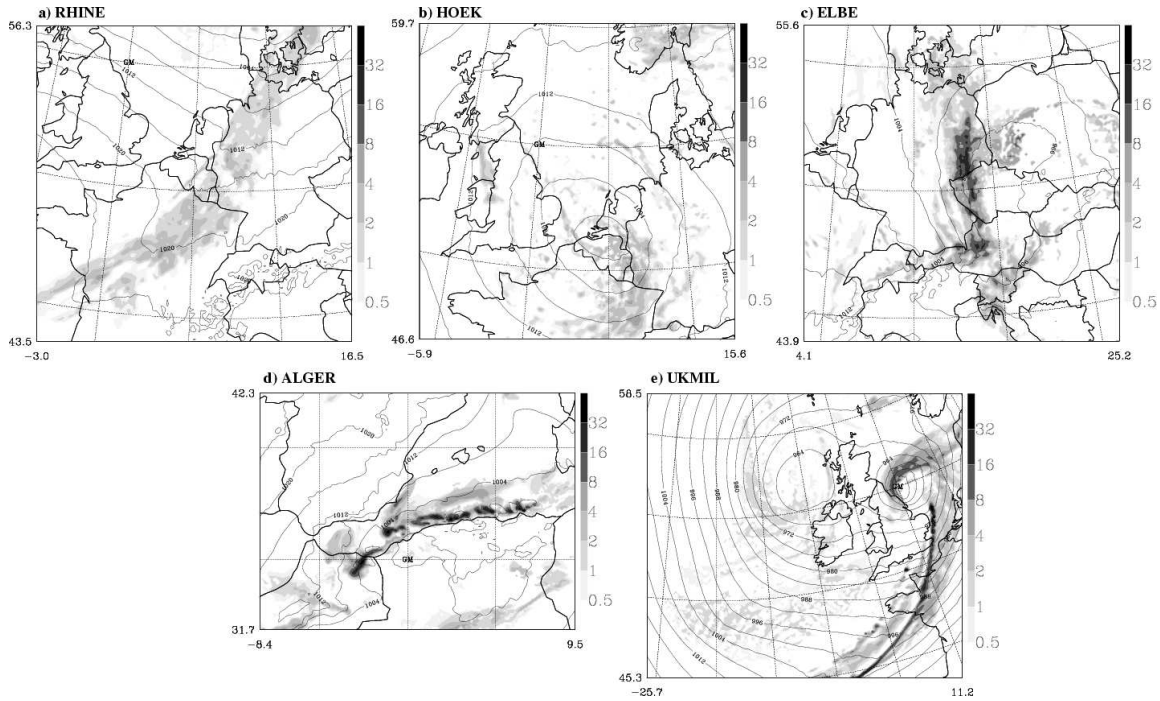

FIG. 2. Surface rainfall (shading; mm h^{-1}) and pressure at mean sea level (contour every 4 hPa) simulated by Meso-NH over the second grid for the various cases and the times corresponding to the nearest hour when an AMSU pass occurred (see Table 2).

sitivity to the shape of the frozen particles is weak in contrast with their other characteristics. The snow scattering properties derived from Liu (2004) were adopted for a good agreement between the simulations and the satellite observations. The model includes a full treatment of the effect of the surface. An emissivity model was implemented for the wind-roughened ocean surface (Guillou et al. 1996). A land surface emissivity atlas derived from SSM/I and AMSU observations was attached to the radiative transfer code (Prigent et al. 2006, 2005, 1997), along with angular and frequency parameterizations.

Note that the BTs can be simulated in the microwave region using RTTOV version 8.7. However, at these frequencies, RTTOV takes only two species of precipitating hydrometeors into account (namely rain and graupel) whereas the BT sensitivity to scattering by snow is dramatic at 89 and 150 GHz. So the snow effects on BTs needed to be analyzed and simulated correctly as in Meirold-Mautner et al. (2007).

3. Case studies

The five cases were typical of midlatitude events. They occurred in autumn, summer, and winter in southern and northern parts of Europe and covered both land and sea. Their associated surface rain rate and pressure at mean sea level are displayed at the AMSU output times in Fig. 2. The cases included a frontal case with light precipitation over the Rhine area (10 February 2000, Fig. 2a), a long lasting precipitation event at Hoek van Holland (19 September 2001, Fig. 2b), a moderate rain case over the Elbe (12 August 2002, Fig. 2c), an intense rain case over Algiers (10 November 2001, Fig. 2d), and the 'millennium storm' in England (30 October 2000, Fig. 2e). All these cases concerned cloud systems organized at the mesoscale.

For the Rhine case (RHINE), light precipitation was related to a cold front passing West Germany on 10 February 2000. At 18 UTC, the cold front was associated with a broad pattern of light surface rainfall of a few mm h^{-1} (Fig. 2a). The 0° C height dropped from 2 to 0.5 km, which was of interest for the precipitation phase retrieval.

Light precipitation occurred on 19 September 2001 at Hoek van Holland (HOEK case). This was a long lasting precipitation event produced by a quasi-stationary low pressure system over the Netherlands (Fig. 2b). A maximum of 100 mm accumulated rainfall was recorded over the whole event at Hoek van Holland, with relatively small rain rates of a few mm h^{-1}.

The Elbe flood (ELBE) case involved convection embedded within synoptic-scale frontal precipitation that resulted in the Elbe flood in August 2002. The synoptic situation was characterized by a deep cyclone moving from the Mediterranean Sea towards Poland (e.g., Zängl 2004). On 12 August, the cyclone was quasi-stationary over eastern Germany and the Czech Republic. On the western side of the low, the partly occluded warm front coincided with the steep-

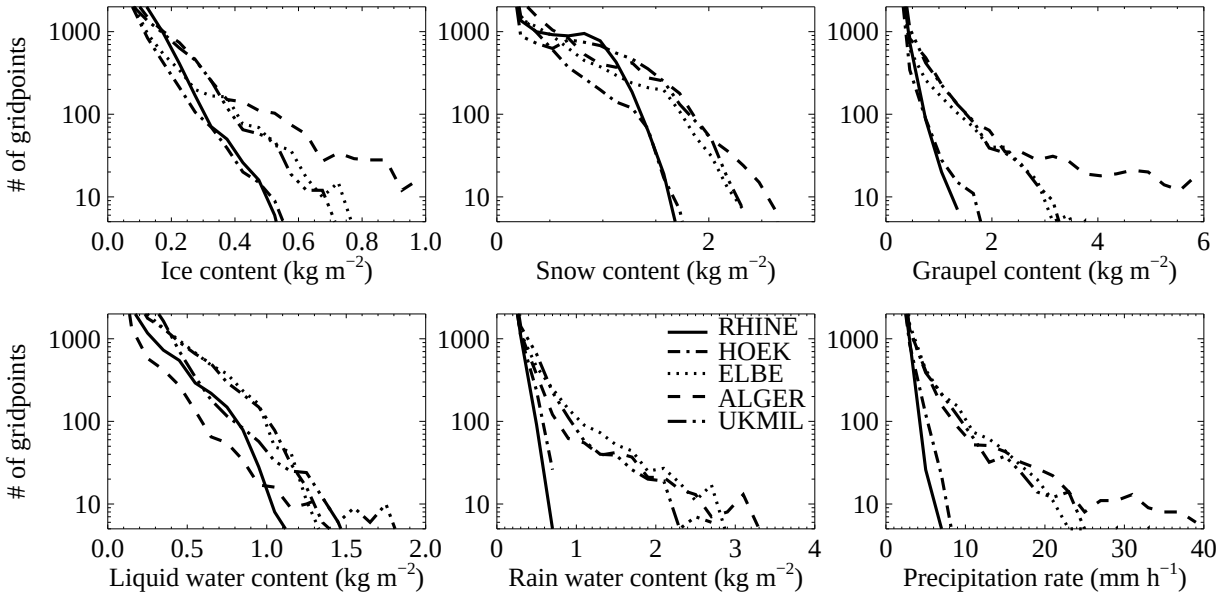

FIG. 3. Distributions of vertically integrated hydrometeor contents (kg m^{-2}) and precipitation rate (mm h^{-1}) for the various cases at the AMSU output times. The bin widths of the ice, snow, graupel, cloud liquid water, and rain water contents, and the precipitation rate are 0.05, 0.15, 0.3, 0.1, 0.2 kg m^{-2} and 2 mm h^{-1}, respectively.

est pressure gradient area at 06 UTC (Fig. 2c). It brought large amounts of rainfall: more than 300 mm fell in one day in parts of Erzgebirge, the mountain range at the German-Czech frontier. The extreme precipitation was followed by a very quick rise of the levels of the Elbe tributaries, leading to a centennial Elbe flood with the largest recorded flood-related damage in Europe.

The Algiers flood case (ALGER) occurred on 10 November 2001 leading to the most devastating flood in this area with more than 700 casualties and catastrophic damage (e.g., Argence et al. 2006; Tripoli et al. 2005). The rainfall was caused by an intense mesoscale cyclone resulting from the interaction between an upper-level trough over Spain and lower-level warm air moving north off the Sahara. At 02 UTC the heaviest rainfalls were located in several cells organized in a line along the North African coast (Fig. 2d). Over Algiers, 262 mm of rainfall was measured during the entire storm episode with more than 130 mm in only 3 hours, between 06 and 09 UTC on 10 November whereas only 41 mm was recorded at the Dar-el-Bedia station, situated inland, only 15 km away from Algiers (Argence et al. 2006).

The 'millennium storm' (UKMIL) corresponded to an exceptionally intense low over the English Midlands and its associated fronts. On 30 October 2000 the low had deepened from 994 to 958 hPa in 12 hours (Browning et al. 2001). The steep pressure gradient resulted in strong winds and widespread gusts between 30 and 40 m s^{-1}. Heavy rain fell all night, leading to 24-hour totals between 25 and 50 mm, with 75 mm and more in some areas. Local floods occurred and caused major disruption of commuter traffic during the morning rush hour of 30 October. The rainfall pattern was typical of an extratropical cyclone at 09 UTC (Fig. 2e). The more intense areas were located in the occluded warm and trailing cold fronts of the low over the North Sea, while weak showers were scattered in the cold sector over the Atlantic Ocean.

4. Cloud and precipitation variability

a. Overview

The distributions of the vertically-integrated hydrometeor contents and the surface precipitation rates are first examined (Fig. 3). For the sake of clarity, the outputs are shown at the AMSU times only. The distribution of the surface precipitation rate shows a large variability that includes light (RHINE and HOEK), moderate (ELBE, UKMIL) and strong (ALGER) precipitation cases, with maximum values of 8, 25, and 40 mm h^{-1}, respectively. The partitioning of the cases into the same three groups was also found for the integrated ice, snow, and graupel contents. In contrast, the distributions of the rain content fell into two groups only (RHINE and HOEK versus ELBE, UKMIL, and ALGER) and the distribution of the liquid water content was more homogeneous. This can be explained by the microphysics and the formation

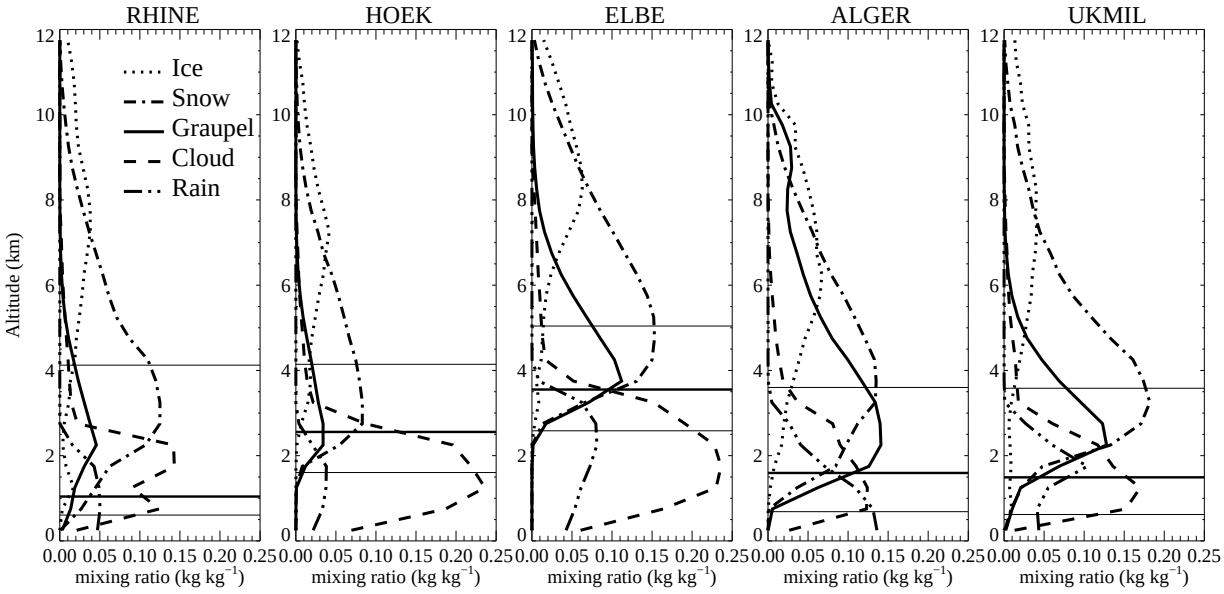

FIG. 4. Mean hydrometeor vertical profiles for the different cases at the AMSU output times. Averages are calculated only from hydrometeor contents taht are not null. The horizontal thick (thin) line represents the mean (extreme) altitude(s) of the 0° C isotherm.

of the hydrometeors. An excess of ice cloud was converted into snow that grew by aggregation and riming and was then transformed into graupel particles. Finally, graupel particles and rain drops contributed the most to the surface precipitation rate.

The surface precipitation rate is the result of a number of complex processes including vertical velocity and humidity supply to the diverse microphysical processes. Therefore the relation between the precipitation rate at the surface and the hydrometeor distribution aloft is not straightforward. An illustration is given in Fig. 4 where the vertical hydrometeor profiles averaged over the simulation domain are drawn. Overall, the distribution of non-precipitating hydrometeors strongly depends on the 0° C isotherm. As the simulation domains cover a few thousands of kilometers, the altitude of the 0° C isotherm changes by a few hundred meters as indicated by the range drawn on each series of profiles (Fig. 4). Non-precipitating ice content is found only above the 0° C isotherm maximum height as the primary ice crystals are immediately melted into cloud droplets at temperatures warmer than 0° C. In contrast, cloud water can exist well above the freezing level in the form of supercooled droplets, which are available for ice riming. Precipitating ice can also be found below the 0° C isotherm in warm layers where the snowflakes are progressively converted into graupel particles which melt as they fall. Rain is formed by autoconversion of cloud droplets or results from the melting of graupel. As a consequence, the rain layer is always below the 0° C isotherm.

The averaged vertical profiles also varied from case to case (Fig. 4). This was mostly due to the seasonal variation of the air temperature. The RHINE case in February included grid points where graupel and snow particles could reach the ground. The two autumn cases (UKMIL and ALGER) presented similar shapes with snow and graupel layers above the ground. The HOEK case in September displayed precipitating frozen hydrometeors higher, above 1.5 km. Finally the ELBE case in August was the warmest case with a deep cloud water layer extending up to 4 km and frozen water content present above 2.5 km.

The series of vertical distributions of Fig. 4 clearly shows that the precipitation was produced by cold processes with the formation of intermediate snow and graupel particles that melted later on into rain. A large number of methods to estimate surface precipitations from microwave observations, especially at high frequencies, are based on the statistical relationship between the upper atmospheric ice particles and the surface precipitation rate (e.g. Ferraro and Marks 1995; Grody 1991; Spencer et al. 1989). Such a relationship was investigated by looking at the correlation between the surface precipitation rate and the different integrated hydrometeor contents at two output times (Fig. 5). As expected, the highest correlation existed with the vertically-integrated rain (up to 0.9). Linear correlation coefficients above 0.7 were also found for the integrated graupel content, but for three cases only. Lower values were obtained for vertically-integrated snow, which were more strongly case-dependent. The correlation relative to the integrated non-precipitating

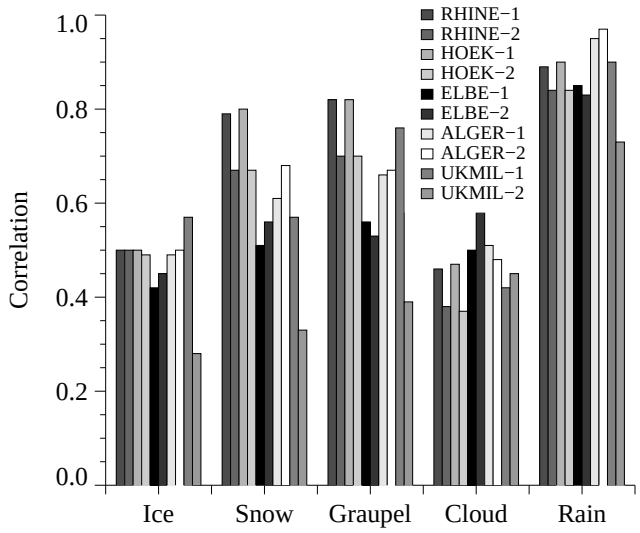

FIG. 5. Correlation of surface precipitation rate with the different integrated hydrometeor contents for the various cases at the two output times.

water (ice and cloud water) contents was the lowest (around 0.5). It should also be pointed out that the correlation values for a particular case and a particular water content can vary considerably with time. For example, the correlation coefficients with the integrated graupel content for the ELBE case were 0.76 and 0.39 at 06 and 18 UTC, respectively. This makes rain retrieval from indirect measurements of cloud and precipitation contents, using regression-based methods, highly challenging.

b. Midlatitude versus tropical databases

The mean vertical profiles of these midlatitude situations differ significantly from those found in tropical conditions. First, the freezing level is located between 1 and 3 km altitude while it is usually as high as 4.5 km in the tropics. This means that the frozen hydrometeors in this database are present at the first levels above the surface. Then, these midlatitude cases are mostly stratiform in nature. Therefore they sample meteorological conditions with weak vertical velocity that favors small-sized hydrometeors (snow and light rain), in contrast to tropical deep convective situations more favorable to the growth of large graupel particles and big rain drops.

An illustration of the difference in characteristics between midlatitude and tropical databases can be seen by comparing the distribution of the current database with the GPROF one. The latter includes six cloud-resolving model simulations in its latest version (four tropical and two midlatitude simulations; Olson et al. 2006). Results are shown in

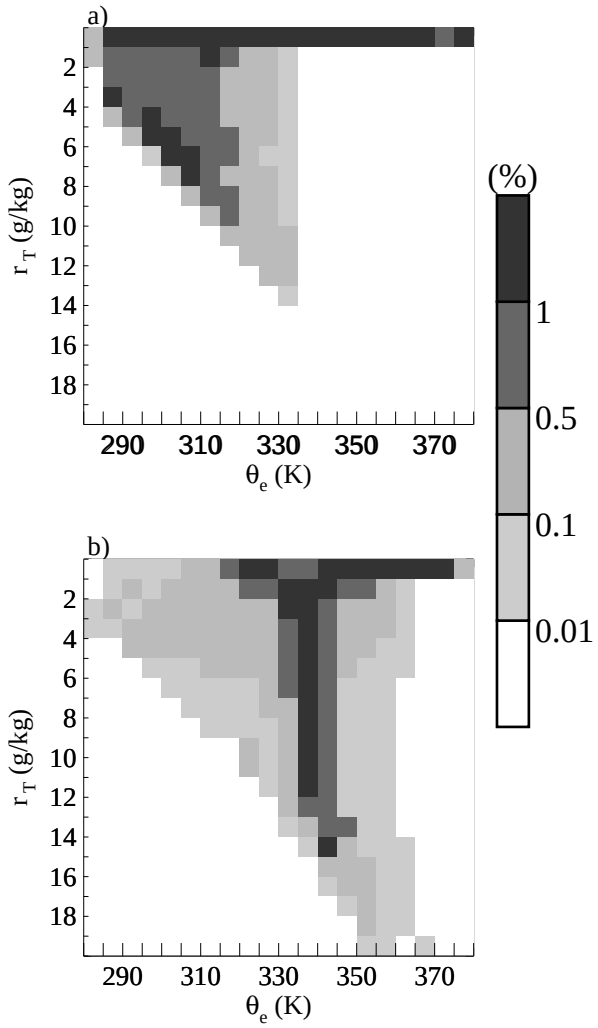

FIG. 6. Conserved-variable (θ_e - r_T) diagrams of the (a) current and (b) GPROF databases obtained from all the tropospheric levels.

a conserved-variable diagram with equivalent potential temperature (θ_e) as abscissa and total water content (r_T) as ordinate obtained from all the tropospheric levels (Fig. 6). This diagram is commonly used for examining mixing processes within clouds. A typical individual sounding presents an r_T that decreases with altitude and a θ_e minimum at midlevels. In the current database, most of the gridpoints display values in the top left corner, with $\theta_e < 330$ K and $r_T < 14$ g kg^{-1} (Fig. 6a). In contrast, the distribution of the GPROF database is shifted towards the bottom-right. In particular, at low altitudes, θ_e and r_T present larger values than the current database, around 350 K and 18 g kg^{-1} respectively (Fig. 6b).

5. Cloud database evaluation

The quality of the simulated cloud and precipitation fields will now be examined. This is done objectively by comparing simulations with satellite observations using the model-to-satellite approach. The frequency ranges considered here record different cloud properties. The 11-μm channel is mainly sensitive to the cloud top temperature. At 37 GHz, emission from cloud liquid water is significant compared to the cold oceanic background. In contrast, the BTs at 150, 89, and 85 GHz decrease with the hydrometeor columns due to scattering by large ice particles (snow and graupel). In the following, an example of observed and simulated BTs is first given. Then the BT distributions of all the cases are compared. Finally two objective verifications of the cloud cover and rain forecasts are performed.

a. Visual inspection of BT maps

As an example, the observed and simulated BTs maps for the ELBE case are shown in Fig. 7. Observations from the 11-μm METEOSAT channel show the high- and middle-level cloud cover with BTs of less than 260 K that rolls around the low centered over central Europe, from Slovakia to Croatia. Elsewhere BTs greater than 260 K mostly result in low-level clouds and clear sky. At 89 and 150 GHz, BTs from AMSU-B of less than 250 K are found over eastern Slovakia and on a line going from eastern Germany to Croatia. These depressed BTs result from significant scattering by large rimed ice particles embedded in the clouds. Note also that snow at the surface yields lower 89-GHz and 150-GHz BTs over the Alps.

The Meso-NH simulation coupled with the radiative transfer codes captures the overall situation as seen in the 11-μm channel well, with high- and middle-level clouds at the right locations. This indicates that the model captures the overall atmospheric circulation. Depressed BTs for the 89-GHz and 150-GHz channels are also simulated correctly over central Europe, but with a smaller extent. The system over eastern Slovakia is almost missing. At 89 and 150 GHz, the surface signature of the cloud-free areas is correctly estimated by the surface climatology over snow and correctly modeled over sea. From the maps for other cases (not shown), similar conclusions can be drawn. The location of the cloud cover as revealed by the 11-μm channel is generally well predicted. The precipitating areas, leading to depressed BTs for the 89-GHz and 150-GHz channels, while less predictable than an extensive cloud cover, present realistic scattered patterns at correct locations.

b. Comparison of BT distribution

The BT comparisons are summarized on BT histograms separated into land and sea surface conditions (Fig. 8). Over land, the grid points at altitudes higher than 1500 m were excluded to filter out the potential presence of snow at the surface. The grid points in the vicinity of coasts were also discarded to avoid large differences due to the contrast of the land/sea surface emissivity in the microwave region. The same flags for land, sea, and coast were applied for both the simulations and the observations. Note also that the satellite BTs at 11-μm (METEOSAT), 150 and 89 GHz (AMSU-B) result from a variable viewing angle while the 37-GHz channel (SSM/I) has a constant viewing angle. Only the vertical polarization of the 37-GHz channel is shown. The simulations are considered for incidence angles corresponding to the satellite observations.

Whatever the case and the surface conditions, the distributions of observed BTs at 11-μm are continuously spread over the 200 and 280 K temperature range (Fig. 8). Two preferential modes are sometimes detectable (e.g. RHINE case) at low and high BTs. They are associated with high-level thick cloud and extended clear sky conditions respectively. At 150 GHz, the observed distributions are highly skewed, leading to peak values between 260 and 280 K over the land, and reduced BTs with a shift of 10-20 K over the sea. A leading edge of minimum BT is also found, with fewer grid points for the light rain cases (RHINE and HOEK). At lower frequencies (89 and 37V GHz), the distributions of observed BTs are also unimodal over land, but with fewer grid points with low BT values. In contrast, over sea, the radiatively cold surface results in BT distributions peaking around 190-210 K. Emission by the hydrometeors explains the presence of some large values of BTs that widen the distributions.

Overall, the simulations reproduce the shape of the BT distributions well for all the channels explored (Fig. 8). The agreement is better over ocean. Over land, some discrepancies can be seen from case to case. For instance, not enough low BTs are simulated at 150 GHz for the ELBE and HOEK cases, whereas the opposite is true for the UKMIL case. At 89 GHz, too many low BTs are simulated for the ELBE and UKMIL cases. This excess of depressed BTs at both frequencies for the UKMIL case suggests an excess of scattering by ice in the simulation. On the other hand, the variation of the discrepancies according to the frequencies for the ELBE case can be attributed to an incorrect representation of the hydrometeors in the meteorological model or to a misinterpretation of their scattering properties in the radiative transfer model.

The realism of the simulated BTs is further demonstrated by the joint BT distributions shown for selected pairs of channels for the observed and simulated data (Fig. 9). For AMSU-B frequencies (Fig. 9, top), the BTs at 90 and 150 GHz over land are distributed along the upper-left part of the diagonal, with less variability for the simulated BTs than the observed ones. at 90 GHz. The BT depression at 150 GHz

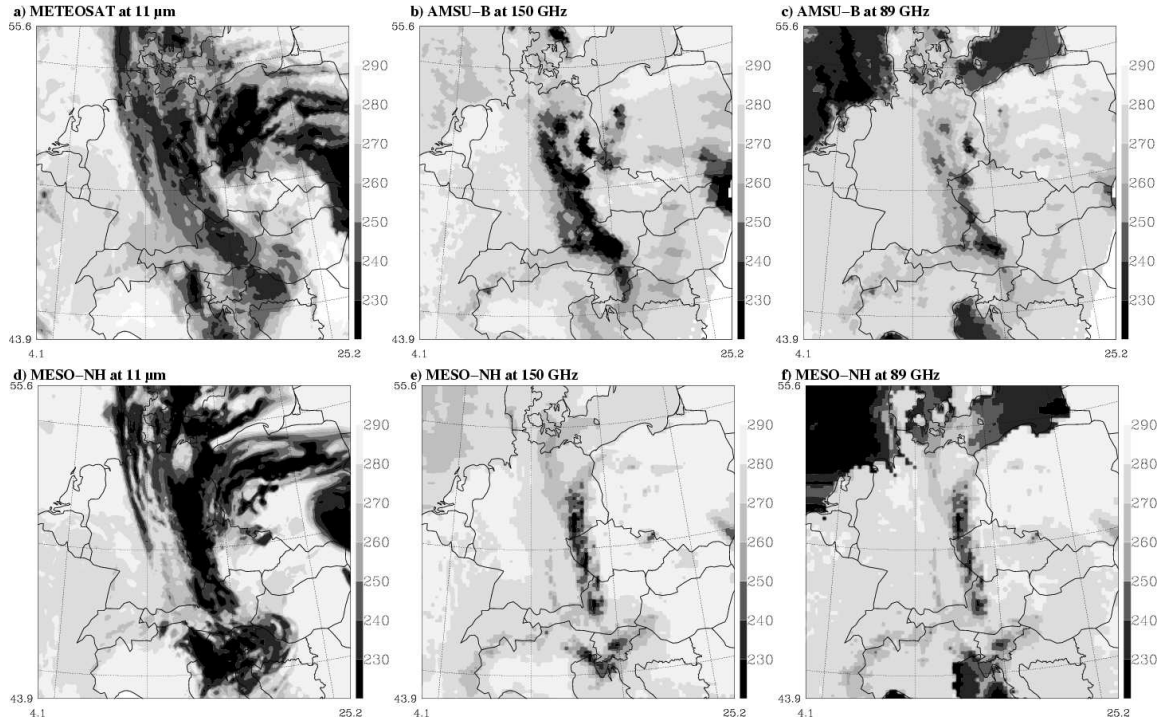

FIG. 7. From left to right, (top) observed and (bottom) simulated BT (K) for the 11-μm, 150-GHz and 89-GHz channels at 07 UTC 12 August 2002 (ELBE case).

can be used as the primary parameter for the retrieval of the ice water path (Liu and Curry 1996). The observed relationship between the 37V and 85V-GHz SSM/I channels (Fig. 9, middle) is also achieved by the simulations both over land and sea. However too BT simulations are too low at 85V GHz; this is due to a few convective cells from the ALGER case (see also Fig. 8). Finally, joint BT distribution of horizontal versus vertical polarization for 37 and 85 GHz SSM/I channels are shown over sea (Fig. 9, bottom). Such a combination of polarizations at 37 and 85 GHz can be used to minimize temperature and surface water effects on the rain-rate retrieval (Conner and Petty 1998). The water surface emission is characterized by low and strongly polarized BT while the effect of precipitation tends to increase BTs and to weaken the polarization difference. This appears to be well reproduced by the simulations at 37 GHz. At 85 GHz, the large depression caused by frozen hydrometeors yields a weak polarization difference for low BT values. This signal was not observed due to the lower resolution of the satellite; therefore such anomalous BTs (from the ALGER case) might be withdrawn from the database for retrieval purposes. This shows that convective cases are a specific challenge that requires further analyses together with more cases to be investigated.

c. Verification of cloud cover and rain forecasts

A further step in the validation is made by the verification of cloud cover and rain forecasts. Here we use categorical scores that measure the correspondence between simulated and observed occurrence of events at grid-points. These scores were first developed to focus on tornado detection and later to verify the occurrence of high precipitation rates (Wilks 1995). In the following, we use the probability of detection (POD), the false alarm ratio (FAR), the probability of false detection (POFD), and the Heidke Skill Score (HSS). POD gives the relative number of times an event was forecast when it occurred, the FAR gives the relative number of times the event was forecast when it did not occur, the POFD is the fraction of no events that were incorrectly forecast as yesr, and the HSS measures the fraction of correct forecasts after eliminating those which would be correct due to chance. Such scores quantify the ability of the model to forecast an event at the right place.

The calculation of scores was first applied to the 11-μm METEOSAT channel, taking advantage of the high temporal resolution of the observations. A threshold of 260 K was chosen to discriminate high- and mid-level thick clouds. The 24-h evolution of the POD and the FAR is shown for the RHINE, HOEK, and ELBE cases (Fig. 10). The comparison is made grid-point by grid-point (gray lines) and area by area (black lines). The calculation area by area compares

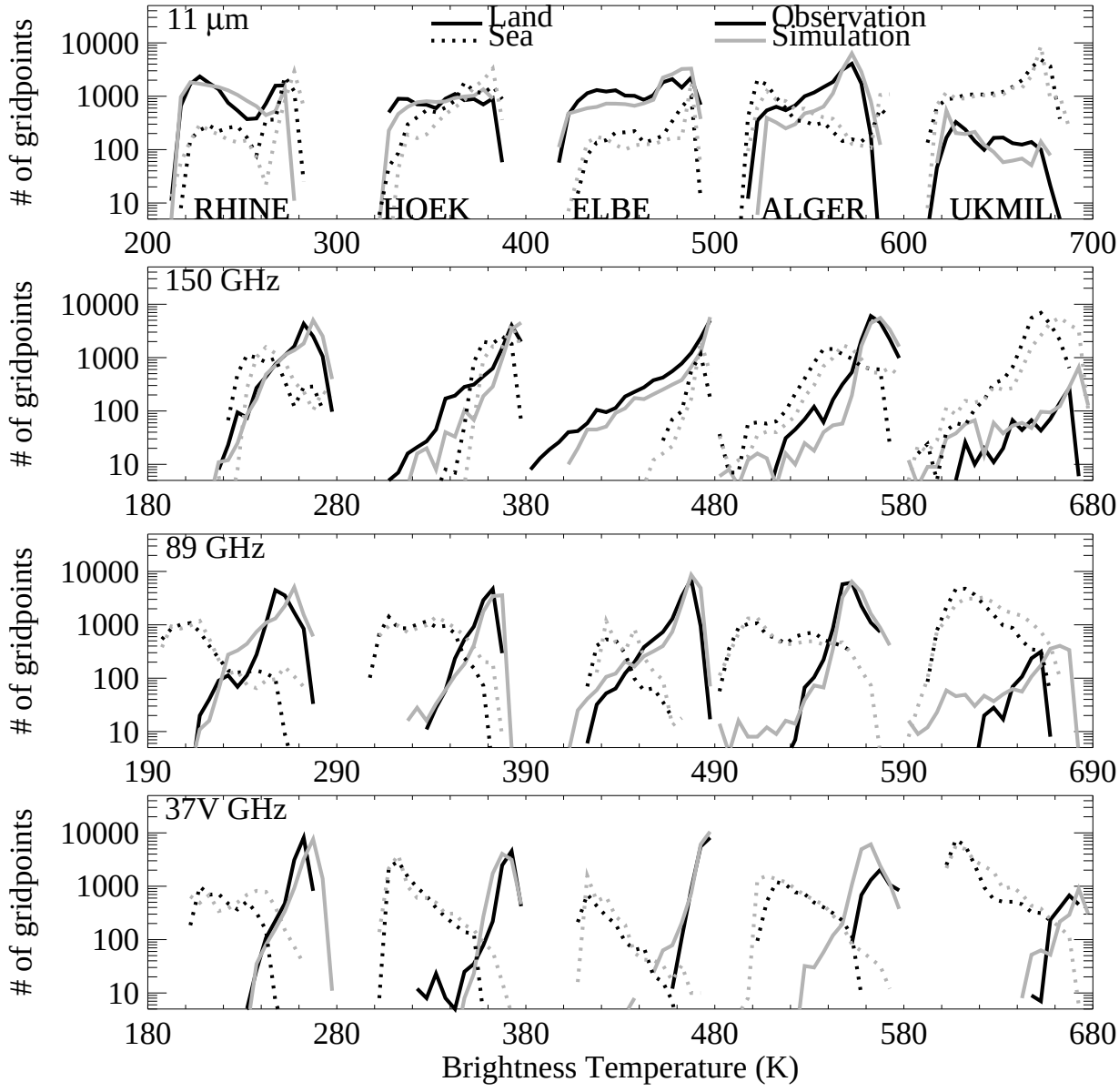

FIG. 8. Observed and simulated BT distributions for the 11 μm, 150, 89 and 37V GHz channels, separated into land and sea grid points for each case. The bin width is 5 K. The BTs are shifted to the right by 0, 100, 200, 300, 400, and 500 K for the RHINE, HOEK, ELBE, ALGER, and UKMIL cases, respectively.

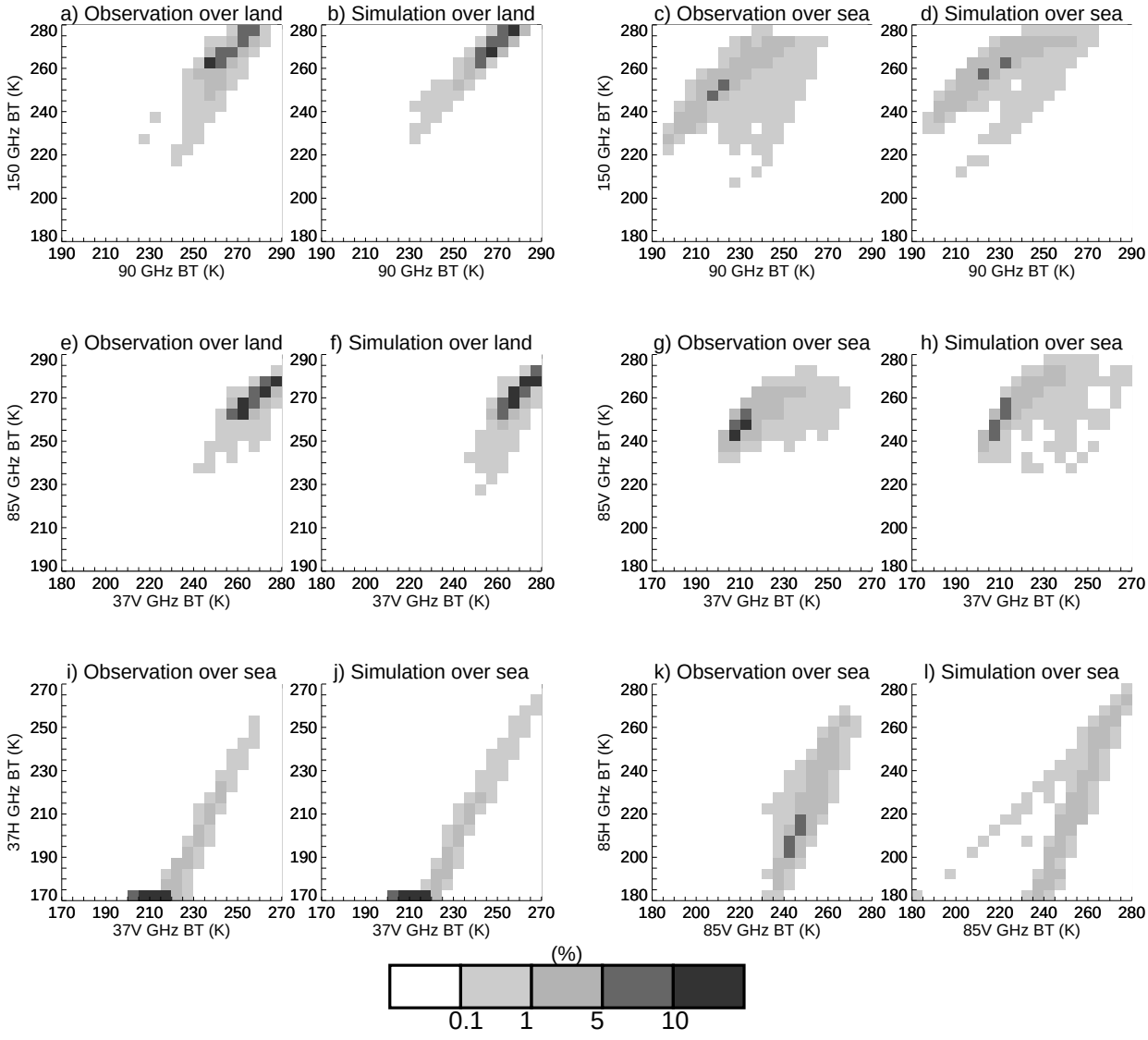

FIG. 9. Observed and simulated joint BT distributions for (top row) the 90 and 150 GHz AMSU channels, (middle row) the 37V and 85V GHz channels, separated into land and sea grid points, and (bottom) the 37V and 37H GHz, and 85V and 85H GHz channels for gridpoints over sea only. The bin width is 5 K.

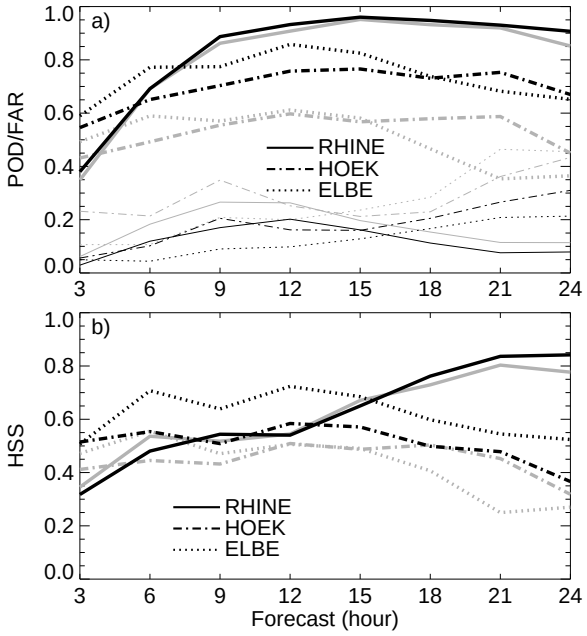

FIG. 10. Time evolution of (a) the POD (thick lines), FAR (thin lines), and (b) HSS of the high-cloud category (11-μm BT $<$ 260 K) calculated for the RHINE, HOEK, and ELBE cases. The grey (black) lines represent the calculation grid-point by grid-point (area by area).

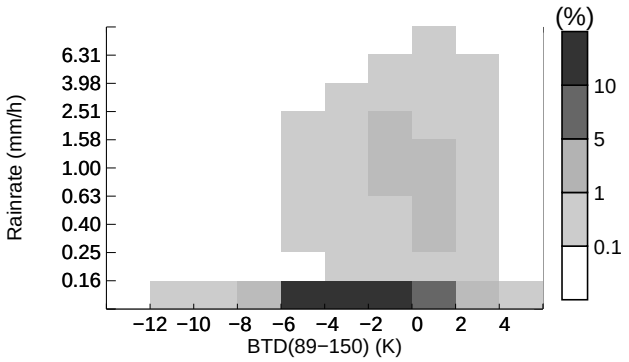

FIG. 11. Distribution of rain rate according to the BTD between the 90- and 150-GHz channels over land.

fractions of occurrence of events over a sized area (Roberts 2005). Such calculation takes the double penalty effect into account. The latter arises when an observed small scale feature is more realistically forecast but is misplaced. Compared to a low resolution model, a high resolution model is penalized twice, once for missing the actual feature and again for forecasting it where it is not. The area used here is a square of five by five grid-points, i.e. areas of 50 km by 50 km that exceed 50% of cloud cover.

For the three cases, when calculated grid-point by grid-point, the POD is generally over 0.5, the FAR is less than 0.5 and the HSS is positive, generally over 0.4. This implies that the simulations have forecasting skill. Overall, the RHINE case gives the best forecast with the largest POD, (almost) the smallest FAR and the largest HSS (at least after 15-h). This was to be expected as the cloud cover of a midlatitude front is the signature of well predicted synoptic scales whereas the two other cases concern two less well organized cloud fields. This is further shown by the results of scores calculated area by area. For the RHINE case, the POD, the FAR and the HSS comparing areas have the same high-skill values as the scores comparing grid-points. In contrast, for the HOEK and ELBE cases, the POD, FAR, and HSS present a significant improvement. This indicates the good skill of the model to forecast the cloud cover on a 50-km scale.

Another application of the scores is to evaluate the skill of the model to detect rainfall over land. Algorithms for the detection of rain over land are usually based on the scattering signal of millimeter-sized ice hydrometeors (e.g. Bennartz et al. 2002; Ferraro et al. 2000). To take advantage of the AMSU-B spatial resolution, we calculated brightness temperature difference (BTD) between 89- and 150-GHz channels, albeit both affected by scattering (in contrast to the common combination of 23 and 89 GHz). The distribution of the rain rate with the BTD for the five simulations is shown in Fig. 11. As discussed by Bennartz et al. (2002), a larger probability of rainfall comes with a larger BTD.

The categorical scores can take this uncertainty into account. A Relative Operating Characteristic (ROC) diagram plots the POD against the POFD using a set of increasing probability thresholds (for BTD decreasing from 4 K to -4 K; Fig. 12). The comparison is made here pixel by pixel. The diagonal line means no skill at all, while the better the classifier, the closer the curve moves to the upper-left corner (high POD with a low POFD). Almost all the points are in the top-left quadrant. This demonstrates the skill of all the simulations to detect BTD events, which by extension means the occurrence of rain events.

The rain forecasts were verified against 24 h accumulated rainfalls measured by rain gauges for the 24-h simulations (RHINE, HOEK, and ELBE). Note that there is a 6-h shift between the 24 h accumulated rainfalls measured at 06 UTC by the rain gauges and those simulated at 00 UTC from the model. The bias range from -12 to -1 mm (or between 20 and 30% in terms of relative bias) and the correlation coefficient is around 0.8 for the ELBE case and around 0.5 for the traveling front cases, the lowest correlation coefficient that can be partly explained by the 6-h shift. These statistics are comparable to those obtained for rain forecast over the Alps

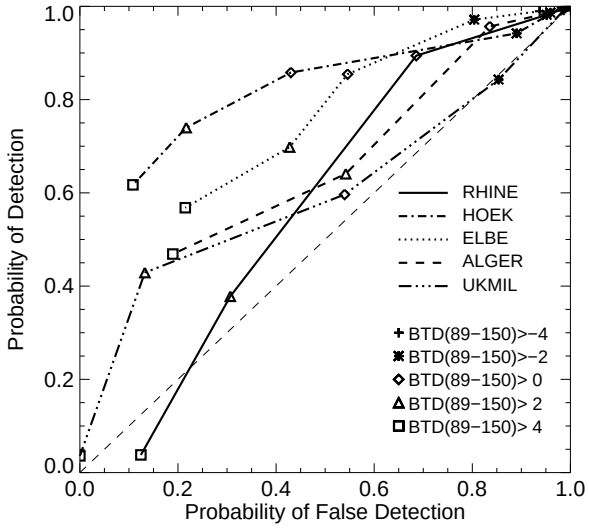

FIG. 12. ROC diagram for BTD between the 90- and 150-GHz channels over land.

(Richard et al. 2007). When comparing categories of accumulated rainfall larger than 1 mm, POD is around 0.85 and FAR around 0. The HSS is around 0.5 that shows the useful skill of the model in forecasting rainfall at the right place.

6. Conclusions

A cloud database of midlatitude situations has been presented. The meteorological cases are typical of the meteorological variability at midlatitudes. They include heavy rain episodes resulting in dramatic floods, but also light precipitation events. They were selected over southern and northern parts of Europe during summer, autumn, and winter seasons. The distribution of the averaged vertical profiles of hydrometeors varies mostly with the 0° C isotherm, located on average between 1 and 3 km height. The database also contains profiles where graupel and snow reach the ground. It thus differs significantly from the GPROF tropical database characterized by a 0° C isotherm located around 4.5 km height. As a result, this database can complement the GPROF base for midlatitude situations. The present midlatitude cloud database is available upon request from the first author.

An evaluation of the simulations has been performed using satellite observations in both the thermal infrared and microwave through a model-to-satellite approach. The comparison is performed on a 10-km grid, which compares with the satellite spatial resolution. Whatever the channels, the observed and simulated BT distributions agree reasonably well for all the cases. As shown by Mech et al. (2007) and Defer et al. (2007), the simulations (the model outputs coupled with the radiative transfer codes) are realistic enough to be used as a cloud database for retrieval purposes.

Then the model-to-satellite approach is combined with the calculation of categorical scores. This allows the prediction of cloud and precipitation occurrence to be checked against satellite observations. In the infrared, the Meso-NH model shows good skill in forecasting cloud cover. In particular, the frontal case (RHINE) displays higher POD and HSS, and lower FAR than the two other cases investigated. This suggests better skill in forecasting synoptic-scale cloud systems. In the microwave region, a current diagnosis based on BTD between 89- and 150-GHz channels is used for rain detection. Despite the non-linear relationship between BTD and rain, the simulations display skill in BTD categories with a varying threshold. In the future, such diagnostic tools could be used in NWP to verify the forecasts of cloud cover and rain all over the globe. Such a tool, that monitors the performance for the cloud scheme in operational systems, would be precious for further developing cloud schemes.

The current database provides physically consistent profiles of cloud, rain, pristine ice, snow, and graupel to be used as inputs to develop rain rate retrieval methods over the midlatitudes. The statistical relationship between cloud and rain profiles and the surface rain rate shows that such an approach can be very challenging when based on satellite measurements that are essentially sensitive to the upper cloud layers. Using the current database, Mech et al. (2007) have shown the ability to retrieve integrated frozen hydrometeor contents with a good accuracy depending on the case. The current database can also be employed for exploring the capability of a submillimeter instrument as reported by Mech et al. (2007) and Defer et al. (2007). In the near future it is planned to add other fully documented case studies to the database. In addition, the evaluation efforts will continue using active instruments like space-borne lidar and radar. These new instruments are well suited to testing the vertical hydrometeor distribution simulated by the Meso-NH model with more accuracy.

Acknowledgment. We thank Chris Kummerow for making the GPROF database available to us and Peter Bechtold for providing us the rain gauge data. This study was supported by EUMETSAT under contract EUM/CO/04/1311/KJG and by ESA under contract 18054/04/NL/FF. Additional support for Eric Defer came from CNES under TOSCA contract 'Etude mission pour la détection et le suivi des nuages de glace dans le domaine submillimétrique'. Nathalie Söhne was supported by a CNES/Météo-France grant. Computer resources were allocated by IDRIS. AMSU data come from the NOAA Satellite Active Archive. METEOSAT observations are copyright 2003 EUMETSAT. The comments of the anonymous reviewers helped us to improve the presentation of the results.

REFERENCES

Argence, S., D. Lambert, E. Richard, N. Söhne, J.-P. Chaboureau, F. Crépin, and P. Arbogast, 2006: High resolution numerical study of the Algiers 2001 flash flood: sensitivity to the upper-level potential vorticity anomaly. *Adv. Geosciences*, **7**, 251–257.

Baran, A. J. and P. N. Francis, 2004: On the radiative properties of cirrus cloud at solar and thermal wavelengths: a test of model consistency using high-resolution airbone radiance measurements. *Quart. J. Roy. Meteor. Soc.*, **130**, 763–778.

Bauer, P., 2001: Over-Ocean Rainfall Retrieval from Multisensor Data of the Tropical Rainfall Measuring Mission. Part I: Design and Evaluation of Inversion Databases. *J. Atmos. Ocean. Tech*, **18**, 1838–1855.

Bechtold, P., E. Bazile, F. Guichard, P. Mascart, and E. Richard, 2001: A mass flux convection scheme for regional and global models. *Quart. J. Roy. Meteor. Soc.*, **127**, 869–886.

Bennartz, R., A. Thoss, A. Dybbroe, and D. B. Michelson, 2002: Precipitation analysis using the Advanced Microwave Sounding Unit in supoort of nowcasting applications. *Meteorol. Atmos. Phys.*, **9**, 177–189.

Browning, K. A., R. S. Dixon, C. Gaffard, and C.-G. Wang, 2001: Wind-profiler measurements in the storm of 30 October 2000. *Weather*, **56**, 367–373.

Caniaux, G., J.-L. Redelsperger, and J.-P. Lafore, 1994: A numerical study of the stratiform region of a fast-moving squall line. Part I: general description and water and heat budgets. *J. Atmos. Sci.*, **51**, 2046–2074.

Chaboureau, J.-P. and P. Bechtold, 2005: Statistical representation of clouds in a regional model and the impact on the diurnal cycle of convection during Tropical Convection, Cirrus and Nitrogen Oxides (TROCCINOX). *J. Geophys. Res.*, **110**, D17 103, doi:10.1029/2004JD005 645.

Chaboureau, J.-P., J.-P. Cammas, J. Duron, P. J. Mascart, N. M. Sitnikov, and H.-J. Voessing, 2007a: A numerical study of tropical cross-tropopause transport by convective overshoots. *Atmos. Chem. Phys.*, **7**, 1731–1740.

Chaboureau, J.-P., J.-P. Cammas, P. Mascart, J.-P. Pinty, C. Claud, R. Roca, and J.-J. Morcrette, 2000: Evaluation of a cloud system life-cycle simulated by Meso-NH during FASTEX using METEOSAT radiances and TOVS-3I cloud retrievals. *Quart. J. Roy. Meteor. Soc.*, **126**, 1735–1750.

Chaboureau, J.-P., J.-P. Cammas, P. Mascart, J.-P. Pinty, and J.-P. Lafore, 2002: Mesoscale model cloud scheme assessment using satellite observations. *J. Geophys. Res.*, **107(D17)**, 4301, doi:10.1029/2001JD000 714.

Chaboureau, J.-P. and J.-P. Pinty, 2006: Evaluation of a cirrus parameterization with Meteosat Second Generation. *Geophys. Res. Lett.*, **33**, L03 815, doi:10.1029/2005GL024 725.

Chaboureau, J.-P., P. Tulet, and C. Mari, 2007b: Diurnal cycle of dust and cirrus over West Africa as seen from Meteosat Second Generation satellite and a regional forecast model. *Geophys. Res. Lett.*, **34**, L02 822, doi:10.1029/2006GL027 771.

Chevallier, F., P. Bauer, G. Kelly, C. Jakob, and T. McNally, 2001: Model clouds over oceans as seen from space: comparison with HIRS/2 and MSU radiances. *J. Climate*, **14**, 4216–4229.

Conner, M. D. and G. W. Petty, 1998: Validation and intercomparison of SSM/I rai-rate retrieval methods over the continental United States. *Geophys. Res. Lett.*, **37**, 679–700.

Cuxart, J., P. Bougeault, and J.-L. Redelsperger, 2000: A turbulence scheme allowing for mesoscale and large-eddy simulations. *Quart. J. Roy. Meteor. Soc.*, **126**, 1–30.

Defer, E., C. Prigent, F. Aires, J.-R. Pardo, C. J. Walden, O.-Z. Zanif, J.-P. Chaboureau, and J.-P. Pinty, 2007: Development of precipitation retrievals at millimeter and submillimeter wavelengths for geostationary satellites. *J. Geophys. Res.*, in revision.

Ferraro, R. R. and G. F. Marks, 1995: The development of SSM/I rain-rate retrieval algorithms using ground-based radar measurements. *J. Atmos. Ocean. Tech*, **12**, 755–770.

Ferraro, R. R., F. Weng, N. C. Grody, and L. Zhao, 2000: Precipitation characteristics over land from the NOAA-15 AMSU sensor. *Geophys. Res. Lett.*, **27**, 2669–2672.

Gregory, D., J.-J. Morcrette, C. Jakob, A. M. Beljaars, and T. Stockdale, 2000: Revision of convection, radiation and cloud schemes in the ECMWF model. *Quart. J. Roy. Meteor. Soc.*, **126**, 1685–1710.

Grody, N. C., 1991: Classification of snow cover and precipitation using the Special Sensor Microwave/Imager (SSM/I). *J. Geophys. Res.*, **96**, 7423–7435.

Guillou, C., S. J. English, and C. Prigent, 1996: Passive microwave airborne measurements of the sea surface response at 89 and 157 GHz. *J. Geophys. Res.*, **101(C2)**, 3775–3788.

Kummerow, C., Y. Hong, W. S. Olson, R. F. Adler, J. McCollumn, R. Ferraro, G. Petty, D.-B. Shin, and T. T. Wilheit, 2001: The evolution of the Goddard profiling algorithm (GPROF) for rainfall estimation from passive microwave sensors. *J. Appl. Meteor.*, **40**, 1801–1820.

Lafore, J.-P., J. Stein, N. Asencio, P. Bougeault, V. Ducrocq, J. Duron, C. Fischer, P. Héreil, P. Mascart, V. Masson, J.-P. Pinty, J.-L. Redelsperger, E. Richard, and J. Vilà-Guerau de Arellano, 1998: The Meso–NH Atmospheric Simulation System. Part I: adiabatic formulation and control simulations. Scientific objectives and experimental design. *Ann. Geophys.*, **16**, 90–109.

Lin, Y.-L., R. D. Farley, and H. D. Orville, 1983: Bulk parameterization of snow field in a cloud model. *J. Climate. Appl. Meteorol.*, **22**, 1065–1092.

Liu, G., 2004: Approximation of single scattering properties of ice and snow particles for high microwave frequencies. *J. Atmos. Sci.*, **61**, 2441–2456.

Liu, G. and J. Curry, 1996: Large-scale cloud features during January 1993 in the North Atlantic Ocean as determined from SSM/I and SSM/T2 observations. *J. Geophys. Res.*, **101**, 7019–7032.

Masson, V., J.-L. Champeaux, C. Chauvin, C. Meriguet, and R. Lacaze, 2003: A global database of land surface parameters at 1 km resolution for use in meteorological and climate models. *J. Climate*, **16**, 1261–1282.

McFarquhar, G. M., S. Iacobellis, and R. C. J. Somerville, 2003: SCM simulations of tropical ice clouds using observationnaly based parameterizations of microphysics. *J. Climate*, **16**, 1643–1664.

Mech, M., S. Crewell, I. Meirold-Mautner, C. Prigent, and J.-P. Chaboureau, 2007: Information content of millimiter observations for hydrometeor properties in mid-latitudes. *IEEE Trans. Geosci. Remote Sensing*, **45**, 2287–2299.

Medaglia, C. M., C. Adamo, F. Baordo, S. Dietrich, S. Di Michele, V. Kotroni, K. Lagouvardos, A. Mugnai, S. Pinori, E. A. Smith, and G. J. Tripoli, 2005: Comparing microphysical/dynamical outputs by different cloud resolving models: impact on passive microwave precipitation retrieval from satellite. *Adv. Geosciences*, **2**, 195–199.

Meirold-Mautner, I., C. Prigent, E. Defer, J. R. Pardo, J.-P. Chaboureau, J.-P. Pinty, M. Mech, and S. Crewell, 2007: Radiative transfer simulations using mesoscale cloud model outputs: comparisons with passive microwave and infrared satellite observations for mid-latitudes. *J. Atmos. Sci.*, **64**, 1550–1568.

Mishchenko, M. I., 1991: Light scattering by size/shape distributions of randomly oriented axially symmetric particles. *J. Opt. Soc. Am. A*, **8**, 871–882.

Morcrette, J.-J., 1991: Evaluation of model-generated cloudiness: Satellite-observed and model-generated diurnal variability of brightness temperature. *Mon. Wea. Rev.*, **119**, 1205–1224.

Noilhan, J. and S. Planton, 1989: A simple parameterization of land surface processes for meteorological models. *Mon. Wea. Rev.*, **117**, 536–549.

Olson, W. S., C. D. Kummerow, S. Yang, G. W. Petty, W.-K. Tao, T. L. Bell, S. A. Braun, Y. Wang, S. E. Lang, D. E. Johnson, and C. Chiu, 2006: Precipitation and latent heating distributions from satellite passive microwave radiometry. Part I: improved method and uncertainties. *J. Appl. Meteor. Climatol.*, **45**, 702–720.

Panegrossi, G., S. Dietrich, F. S. Marzano, A. Mugnai, E. A. Smith, X. Xiang, G. J. Tripoli, P. K. Wang, and J. P. V. Poiares Baptista, 1998: Use of cloud model microphysics for passive microwave-based precipitation retrieval: Significance of consistency between model and measurement manifolds. *J. Atmos. Sci.*, **55**, 1644–1673.

Pardo, J. R., J. Cernicharo, and E. Serabyn, 2001: Atmospheric Transmission at Microwaves (ATM): An Improved Model for mm/submm applications. *IEEE Trans. on Antennas and Propagation*, **49/12**, 1683–1694.

Pinty, J.-P. and P. Jabouille, 1998: A mixed-phase cloud parameterization for use in a mesoscale non-hydrostatic model: simulations of a squall line and of orographic precipitations. *Proc. AMS conference on cloud physics, 17-21 August 1998, Everett, Wa, USA*, 217–220.

Prigent, C., F. Aires, and W. B. Rossow, 2006: Land surface microwave emissivities over the globe for a decade. *Bull. Amer. Meteor. Soc.*, **87**, 1573–1584.

Prigent, C., F. Chevallier, F. Karbou, P. Bauer, and G. Kelly, 2005: AMSU-A land surface emissivity estimation for numerical weather prediction assimilation schemes. *J. Appl. Meteor.*, **44**, 416–426.

Prigent, C., J. R. Pardo, M. I. Mishchenko, and W. B. Rossow, 2001: Microwave polarized signatures generated within cloud systems: SSM/I observations interpreted with radiative transfer simulations. *J. Geophys. Res.*, **106**, 28 243–28 258.

Prigent, C., W. B. Rossow, and E. Matthews, 1997: Microwave land surface emissivities estimated from SSM/I observations. *J. Geophys. Res.*, **102**, 21 867–21 890.

Richard, E., A. Buzzi, and G. Zngl, 2007: Quantitative precipitation forecasting in the Alps: The advances achieved by the Mesoscale Alpine Programme. *Quart. J. Roy. Meteor. Soc.*, **133**, 831–846.

Roberts, N., 2005: An investigation of the ability of a storm scale configuration of the Met Office NWP model to predict flood producing rainfall. Tech. rep., UKMO Forecasting Research Technical Report No. 455.

Saunders, R., M. Matricardi, P. Brunel, S. English, P. Bauer, U. O'Keeffe, P. Francis, and P. Rayer, 2005: RTTOV-8 Science and validation report. Tech. rep., NWP SAF Report, 41 pages.

Spencer, R. W., H. M. Goodman, and R. E. Hood, 1989: Precipitation retrieval over land and ocean with SSM/I: Identification and characteristics of the scattering signals. *J. Atmos. Ocean. Tech*, **6**, 254–273.

Stein, J., E. Richard, J.-P. Lafore, J.-P. Pinty, N. Asencio, and S. Cosma, 2000: High-resolution non-hydrostatic simulations of flash-flood episodes with grid-nesting and ice-phase parameterization. *Meteorol. Atmos. Phys.*, **72**, 203–221.

Tripoli, G. J., C. M. Medaglia, S. Dietrich, A. Mugnai, G. Panegrossi, S. Pinori, and E. A. Smith, 2005: The 9-10 November 2001 Algerian flood: A numerical study. *Bull. Amer. Meteor. Soc.*, **86**, 1229–1235.

Wiedner, M., C. Prigent, J. R. Pardo, O. Nuissier, J.-P. Chaboureau, J.-P. Pinty, and P. Mascart, 2004: Modeling of passive microwave responses in convective situations using outputs from mesoscale models: comparison with TRMM/TMI satellite observations. *J. Geophys. Res.*, **109**, D06 214, doi:10.1029/2003JD004 280.

Wilks, D. S., 1995: *Statistical Methods in the Atmospheric Sciences*. Academic Press, 467 pp.

Zängl, G., 2004: Numerical simulations of the 12–13 August 2002 flooding event in eastern Germany. *Quart. J. Roy. Meteor. Soc.*, **130**, 1921–1940.

Printed August 21, 2007.